The Astrophysical Journal Letters, 881:L5 (5pp), 2019 August 10 https://doi.org/10.3847/2041-8213/ab31f8

Building Up Solar-wind-like 3D Uniform-intensity Magnetic Fields

Francesco Valentini[1], Francesco Malara[1], Luca Sorriso-Valvo[2,3], Roberto Bruno[4], and Leonardo Primavera[1]
[1] Dipartimento di Fisica, Università della Calabria, ponte P. Bucci, cubo 31C, I-87036, Rende (CS), Italy; francesco.malara@fis.unical.it
[2] Departamento de Física, Escuela Politécnica Nacional, 170517 Quito, Ecuador
[3] Nanotec/CNR, U.O.S. di Cosenza, ponte P. Bucci, cubo 31C, I-87036, Rende (CS), Italy
[4] INAF IFSI-Roma, via Fosso del Cavaliere 133, I-00133, Roma, Italy
Received 2019 June 10; revised 2019 June 27; accepted 2019 July 11; published 2019 August 5

Abstract

A numerical model representing a 3D turbulent constant-magnitude magnetic field $\boldsymbol{B}$ is described. Assuming a form for two components of the vector potential, the third component is calculated such as to obtain a uniform intensity for $\boldsymbol{B}$. Singular surfaces are always present in the solution, in the form of rotational discontinuities. Using a spectrum for derivatives of the given vector potential components that satisfies the critical-balance condition, an anisotropic spectrum for $\boldsymbol{B}$ is obtained, with a prevalence of perpendicular wavevectors $k_\perp$ and a Kolmogorov power-law range with respect to $k_\perp$. These features make the model suitable to represent magnetic turbulence in solar wind fast-speed streams.

Key words: magnetic fields – solar wind – turbulence

1. Introduction

Since the early work by Belcher & Davis (1971), in situ measurements performed in low-latitude fast-speed streams (e.g., Bruno et al. 1985), as well as in the polar wind (Bavassano et al. 2000a; Matteini et al. 2014, 2015), have revealed magnetic field $\delta\boldsymbol{B}$ and plasma velocity $\delta\boldsymbol{v}$ large-amplitude fluctuations with peculiar properties. These include: (i) a $\delta\boldsymbol{v}$–$\delta\boldsymbol{B}$ correlation with the sign corresponding to Alfvén waves propagating outward from the Sun; (ii) low-level magnetic field intensity $\delta|\boldsymbol{B}|$ and plasma density $\delta\rho$ fluctuations; and (iii) a broadband fluctuation spectrum covering several decades (e.g., Bruno & Carbone 2013). The alignment of the magnetic field minimum variance direction with the mean field (Belcher & Davis 1971) is related with the condition $|\boldsymbol{B}| \sim$ const (Barnes 1981). Large-amplitude Alfvén waves tend to evolve toward a state characterized by $|\boldsymbol{B}| \sim$ const (Vasquez & Hollweg 1998), along with embedded rotational discontinuities (Cohen & Kulsrud 1974; Malara & Elaoufir 1991). Nonlinear saturation of the firehose instability also produces a state with nearly constant $|\boldsymbol{B}|$ (Tenerani & Velli 2018). The nearly constancy of $|\boldsymbol{B}|$ also influences the magnetic spectrum index at very large scales (Matteini et al. 2018; Bruno et al. 2019). The above properties of fast-stream fluctuations are more evident at smaller heliocentric distances R, while $\delta\boldsymbol{v}$–$\delta\boldsymbol{B}$ correlation reduces (Bavassano et al. 2000a, 2000b) and $\delta|\boldsymbol{B}|/|\boldsymbol{B}|$ increases with increasing R, possibly due to a parametric decay of Alfvénic fluctuations (Malara & Velli 1996; Malara et al. 2000, 2001; Del Zanna 2001; Matteini et al. 2010; Tenerani & Velli 2013; Del Zanna et al. 2015; Shoda et al. 2018).

The condition $|\boldsymbol{B}| \sim$ const is verified in arc-polarized Alfvén waves (Barnes & Hollweg 1974; Tsurutani & Ho 1997), where $\boldsymbol{B}$ moves along an arc lying on a plane that is perpendicular to the propagation direction. Arc-polarized waves represent ∼10% of Alfvénic modes in low-latitude solar wind (Riley et al. 1996). More generally, in solar wind Alfvénic fluctuations $\boldsymbol{B}$ moves on a spherical surface (Bruno et al. 2004) and probably depends on three independent coordinates.

In many occasions, such as initializing numerical simulations (Rosales & Meneveau 2006), describing processes on broad spatial scale ranges (Sardina et al. 2015), or understanding scaling properties of turbulence (Juneja et al. 1994), the availability of 3D fields reproducing the main features of turbulence may be necessary. This can be done through synthetic turbulence models that reproduce the required features of turbulence with computational requirements that are much lower than direct simulations.

We want to get an explicit synthetic expression of a 3D solenoidal vector field with a uniform intensity and a broadband spectrum, representing the typical magnetic configuration of fast solar wind. While this is easier to do 1D (e.g., Malara & Velli 1996) or 2D (Primavera et al. 2019), it is more difficult for a fully 3D configuration, due to the double constraint $|\boldsymbol{B}| =$ const and $\nabla \cdot \boldsymbol{B} = 0$. Roberts (2012) developed a method in which a solenoidal vector field with a prescribed spectrum is built, with phases of Fourier harmonics chosen to minimize variations of $|\boldsymbol{B}|$. Results have been presented in the 1D case, which probably requires a lower computational effort than in 3D. The resulting synthetic field contains layers where $\boldsymbol{B}$ undergoes rapid variations that are similar to rotational discontinuities observed in the solar wind. This seems to be related to the condition $|\boldsymbol{B}| \simeq$ const. In fact, while the minimization procedure reduces the rms $\delta|\boldsymbol{B}|$, rapid rotations become sharper. The resulting field magnitude is only approximately constant, being $\delta|\boldsymbol{B}|/|\boldsymbol{B}| \simeq 7\%$ (Roberts 2012).

In this Letter we present a new method to generate a fully 3D solenoidal vector field $\boldsymbol{B}$ satisfying the condition $|\boldsymbol{B}| =$ const to a better approximation than in Roberts (2012), and using modest computational effort. In our solution rotational discontinuities spontaneously develop, confirming the idea that such features observed in the solar wind turbulence are strictly related to the uniformity of the magnetic field magnitude.

2. The Method

Our method aims at building a vector field $\boldsymbol{B}(x, y, z)$ that satisfies the conditions (a) $\nabla \cdot \boldsymbol{B} = 0$, and (b) $|\boldsymbol{B}(x, y, z)| = B_T$, with B_T a constant, in a finite spatial domain $D = \{(x, y, z)\} = [0, L_x] \times [0, L_y] \times [0, L_z]$. Condition (a) is fulfilled by expressing $\boldsymbol{B}$ in terms of a vector potential $\boldsymbol{A}(x, y, z)$: $\boldsymbol{B} = \nabla \times \boldsymbol{A}$. Therefore, we have to determine

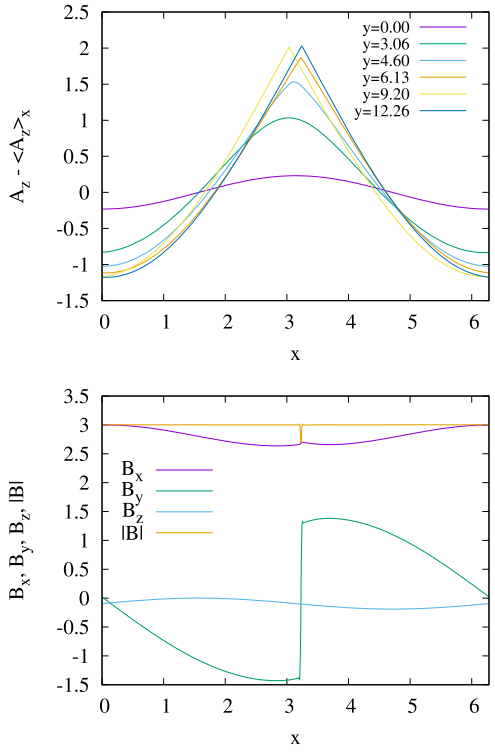

Figure 1. Case A. Top panel: profiles of $A_z - \langle A_z \rangle_x$ as functions of x, for various values of y, and at $z = 0.78$. Bottom panel: profiles of B_x, B_y, B_z, and $|\boldsymbol{B}|$ as functions of x, at $y = 6.13$ and $z = 0.78$.

$\boldsymbol{A}(x, y, z)$ such as to satisfy the condition (b). This is verified if

$$\frac{\partial A_z}{\partial y} = \frac{\partial A_y}{\partial z} + \sqrt{B_T^2 - \left(\frac{\partial A_x}{\partial z} - \frac{\partial A_z}{\partial x}\right)^2 - \left(\frac{\partial A_y}{\partial x} - \frac{\partial A_x}{\partial y}\right)^2} \quad (1)$$

where $\boldsymbol{A} = A_x\hat{\boldsymbol{x}} + A_y\hat{\boldsymbol{y}} + A_z\hat{\boldsymbol{z}}$, and $\hat{\boldsymbol{x}}$, $\hat{\boldsymbol{y}}$, and $\hat{\boldsymbol{z}}$ are the unit vectors in the direction of the Cartesian axes. We assume that $A_x(x, y, z)$ and $A_y(x, y, z)$ are known functions of the coordinates, and we use the nonlinear Equation (1) to determine $A_z(x, y, z)$. Equation (1) is supplemented by a condition at the boundary $y = 0$:

$$A_z(x, 0, z) = a_z(x, z), \quad x \in [0, L_x], \quad z \in [0, L_z] \quad (2)$$

where $a_z(x, z)$ is a known function, while periodicity is assumed along x and z.

To calculate A_z we set up a numerical procedure. We define a regular spatial grid in the domain D $\{(x_i, y_j, z_n)\}$ formed by $N_x \times N_y \times N_z$ points; any known function is calculated at gridpoints. For any value z_n, A_z is calculated at all gridpoints, starting from the boundary condition (2) at $y_1 = 0$ and increasing y step by step ($y_j \rightarrow y_{j+1}$): (a) knowing the solution A_z along a "row" at a given y_j, we calculate $\partial A_z/\partial x$ by a second-order centered finite-difference scheme (FDS); (b) from Equation (1) we obtain $\partial A_z/\partial y$ along the same row y_j; (c) A_z is calculated at y_{j+1} by a second-order FDS, using $\partial A_z/\partial y$ at y_j and A_z at y_{j-1}; a first-order FDS is used for the first step $j = 1$, because only the boundary condition $a(x_i, z_n)$ is available to calculate A_z at the second row y_2. The above procedure is recursively applied, until A_z is calculated at all rows y_j.

With increasing y, the solution A_z tends to develop singularities in form of discontinuities in first-order derivatives. When such a singularity is formed the FDS cannot accurately describe the solution and spurious oscillations are generated around the singular point. Therefore, at each step y_j we smoothed the solution using the following procedure: (i) a low-pass filter is applied to $A_z(x_i, y_j, z_n)$, which reduces the amplitude of the highest k_x Fourier harmonics (Lele 1992), obtaining the filtered solution $A_F(x_i, y_j, z_n)$; (ii) a three-point current average is calculated: $A_{CA}(x_i, y_j, z_n) = [A_F(x_{i+1}, y_j, z_n) + A_F(x_i, y_j, z_n) + A_F(x_{i-1}, y_j, z_n)]/3$; (iii) $A_z(x_i, y_j, z_n)$ is replaced by the smoothed solution $A_S(x_i, y_j, z_n) = q\,A_{CA}(x_i, y_j, z_n) + (1 - q)\,A_F(x_i, y_j, z_n)$, where the parameter q is chosen in the interval $[0, 1]$. The above procedure improves numerical stability by smoothing singularities.

The quantity in the square root of Equation (1) must be nonnegative; therefore, for any given value of the constant B_T, the amplitudes of A_x, A_y, and a_z must be chosen such as to fulfill this condition. Finally, we notice that neither the resulting A_z nor its partial derivatives are periodic along y, though they are periodic along x and z.

3. Results

In order to illustrate the properties of the solution and the formation of a singularity, we first considered a case (Case A) where A_x, A_y, and the boundary condition (2) have simple sinusoidal forms: $A_x = A_0 \sin(y)\sin(z)$, $A_y = -A_0 \cos(x)\sin(z)$, $a_z = -A_0 \cos(x)\cos(z)$, with $A_0 = 0.25$, $B_T = 3$, $L_x = L_z = 2\pi$, $L_y = 4\pi$. Numerical parameters are $N_x = 1024$, $N_y = 4096$, $N_z = 16$, and $q = 1$. In Figure 1 (top panel) profiles of $A_z - \langle A_z \rangle_x$ are plotted as functions of x, for different values of y and $z = 0.78$. The x-average $\langle A_z \rangle_x$ has been subtracted to remove the offset due to a systematic increase of A_z with y. We see that with increasing y the initial sinusoidal profile of A_z is gradually distorted until a singular point appears, where the derivative $\partial A_z/\partial x$ is discontinuous. Further increasing y, the singular point moves at different x positions, thus generating a discontinuity that is also in the derivative $\partial A_z/\partial y$. Starting from the position $y = 0$ where the solution is regular, the singularity develops over a distance ($y \sim 6$), which is of the order of the typical wavelength. This singularity is found also for other values of z, indicating that a singular surface is present in the 3D structure of A_z. At the singular surface the components B_x and B_y are discontinuous, therefore the surface represent a current sheet. In contrast, the component $B_z = \partial A_y/\partial x - \partial A_x/\partial y = A_0[\sin(x) - \cos(y)]\sin(z)$ is regular in the whole domain. In Figure 1 (bottom panel) the profiles of the magnetic field components and of $|\boldsymbol{B}|$ are plotted as functions of x, for $y = 6.13$ and $z = 0.78$. The presence of the discontinuity is clearly visible, mainly in the B_y profile. The profile of $|\boldsymbol{B}|$ is remarkably constant, except for a dip localized at the singular point. In fact, the constancy of $|\boldsymbol{B}|$ is guaranteed by Equation (1), while the smoothing procedure, which modifies the "ideal" solution mostly around the singular point, represents an additional element that does not allow the solution A_z to exactly satisfy Equation (1).

To study a situation that is closer to the solar wind turbulence, in Case B we considered more complex forms for $A_x(x, y, z)$, $A_y(x, y, z)$, and $a_z(x, z)$ that have 3D power-law spectra (2D for a_z). For the evaluation of these quantities, we used a synthetic turbulence model (STM) introduced by Malara et al. (2016) and already employed in modeling magnetic turbulence (Pucci et al. 2016; Perri et al. 2017). The STM builds up a turbulent field as a superposition of localized

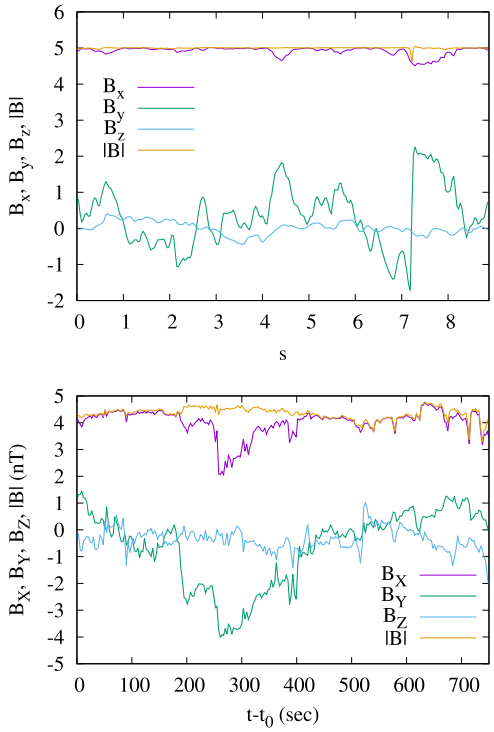

Figure 2. Case B. Top panel: profiles of B_x, B_y, B_z, and $|\boldsymbol{B}|$ as functions of the spatial coordinate s, at $y = 5.65$. Bottom panel: profiles of B_X, B_Y, B_Z, and $|\boldsymbol{B}|$ as functions of time, from the data set of the *Wind* spacecraft (Wicks et al. 2013).

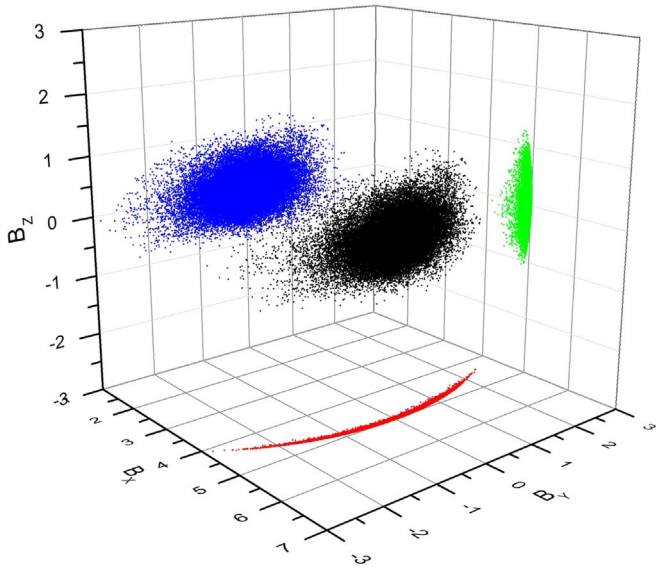

Figure 3. 3D scatter plot of a subset of 50,000 $\boldsymbol{B}$ vector tip positions (black); projections onto coordinate planes (colors).

fluctuations with different amplitudes at different logarithmically distributed spatial scales. The model can reproduce an anisotropic spectrum (Malara et al. 2016) that follows the critical-balance scaling law $\ell_{\parallel} \propto \ell_{\perp}^{2/3}$ (Goldreich & Sridhar 1995), where $\ell_{\parallel}$ and $\ell_{\perp}$ are the perturbation scale lengths parallel and perpendicular to the mean magnetic field $\langle \boldsymbol{B} \rangle$, respectively. Using the STM, we generated A_x, A_y and the boundary condition a_z in the scale ranges $\pi \leqslant \ell_{\perp} \leqslant \pi/32$, $\pi \leqslant \ell_{\parallel} \leqslant \pi/(32^{2/3})$. On average, the amplitude $\tilde{A}_i[\ell_{\parallel}(\ell_{\perp}), \ell_{\perp}]$ of a fluctuation in the spectrum of the vector potential ith component scales as $\tilde{A}_i \propto \ell_{\perp}^{(h+1)}$. For $h = 1/3$ the spectrum of the spatial derivatives of $A_i(x, y, z)$ has a Kolmogorov index ($\propto k_{\perp}^{-5/3}$) in the perpendicular directions, while $\propto k_{\parallel}^{-2}$ in the parallel direction. We choose the parallel direction along x, which is approximately the direction of $\langle \boldsymbol{B} \rangle$ (see below). The STM can also reproduce intermittency through a p-model technique (Meneveau & Sreenivasan 1987); in the present case we used $p = 0.5$, corresponding to no intermittency. A more detailed description of the STM can be found in Malara et al. (2016). We point out that the quantities A_x, A_y, and a_z could also be generated using a different technique, e.g., a 3D FFT. The remaining component A_z is calculated as explained above.

Here we show results obtained using $B_T = 5$, $L_x = L_y = L_z = 2\pi$, $N_x = N_z = 256$, $N_y = 512$, and $q = 0.5$. In Figure 2 (top panel) profiles of B_x, B_y, B_z, and $|\boldsymbol{B}|$ are plotted along a line parallel to the xz plane ($y = 5.65$) that forms a 45° angle with the x direction; s is the spatial coordinate along such a line. This trajectory simulates a spacecraft crossing at heliocentric distance $\simeq$1 au where the Parker spiral forms and angle $\sim$45° with the radial direction. The $\boldsymbol{B}$ components display an irregular behavior, typical of a turbulent field. The average values of the $\boldsymbol{B}$ components over the entire 3D spatial domain are, respectively: $\langle B_x \rangle = 4.96$, $\langle B_y \rangle \sim 10^{-15}$, and $\langle B_z \rangle = 3.77 \times 10^{-4}$; therefore, the mean magnetic field $\langle \boldsymbol{B} \rangle$ is essentially in the x direction. The rms values of the fluctuations for the three components are $\delta B_x = 6.1 \times 10^{-2}$, $\delta B_y = 0.57$, and $\delta B_z = 0.28$. The minimum variance direction is along $\langle \boldsymbol{B} \rangle$, in accordance with the prediction by Barnes (1981) for a uniform-magnitude magnetic field. The different values found for δB_y and δB_z are due to intrinsic asymmetries of the model, and are not fully consistent with a more gyrotropic solar wind turbulence (Saur & Bieber 1999).

The normalized rms fluctuation amplitude is $\delta B/B_T = [(\delta B_x)^2 + (\delta B_y)^2 + (\delta B_z)^2]^{1/2}/B_T = 0.13$; however, the fluctuation amplitude reaches higher values at particular locations, where $[\sum_i (B_i - \langle B_i \rangle)^2]^{1/2}/B_T \sim 1$. Equation (1) requires that $\max\{B_y^2 + B_z^2\} \leqslant B_T^2$. Because in most of the domain it is $B_y^2 + B_z^2 \ll B_T^2$, Equation (1) implies that the direction of the mean field is along x. Figure 2 shows some abrupt jumps (discontinuities), mainly visible in the B_y profile, which have been generated in a similar fashion as in case A, and partially smoothed by numerical effects. Such structures, which are not present in B_z (directly determined by the STM), are consequences of the condition $|\boldsymbol{B}| = \text{const}$ imposed through the nonlinear Equation (1). From Figure 2 we see that $|\boldsymbol{B}|$ remains almost constant, except for small oscillations localized at discontinuities and due to localized violations of the condition (1) produced by the smoothing procedure. However, the normalized rms fluctuation of $|\boldsymbol{B}|$ is quite small: $\delta|\boldsymbol{B}|/B_T = [\langle |\boldsymbol{B}|^2 \rangle - \langle |\boldsymbol{B}| \rangle^2]^{1/2}/B_T \simeq 1.47 \times 10^{-3}$, indicating a substantial constancy of $|\boldsymbol{B}|$ throughout the whole spatial domain. The relative variation of magnetic energy is also very small: $\Delta E_M/E_{M0} = (E_{M0} - E_M)/E_{M0} \simeq 2 \times 10^{-6}$, where $E_M = \int [B^2/(8\pi)]dV$ and $E_{M0} = \int [B_T^2/(8\pi)]dV$.

In the lower panel of Figure 2 the magnetic field components and intensity are plotted, corresponding to a sample of data extracted from the 3 s *Wind* spacecraft data set, where the initial time t_0 corresponds to 2008 January 15, 17:45:00 (Wicks et al. 2013). For an easier comparison with the results of our model, the reference frame in the data set has been rotated so that the X

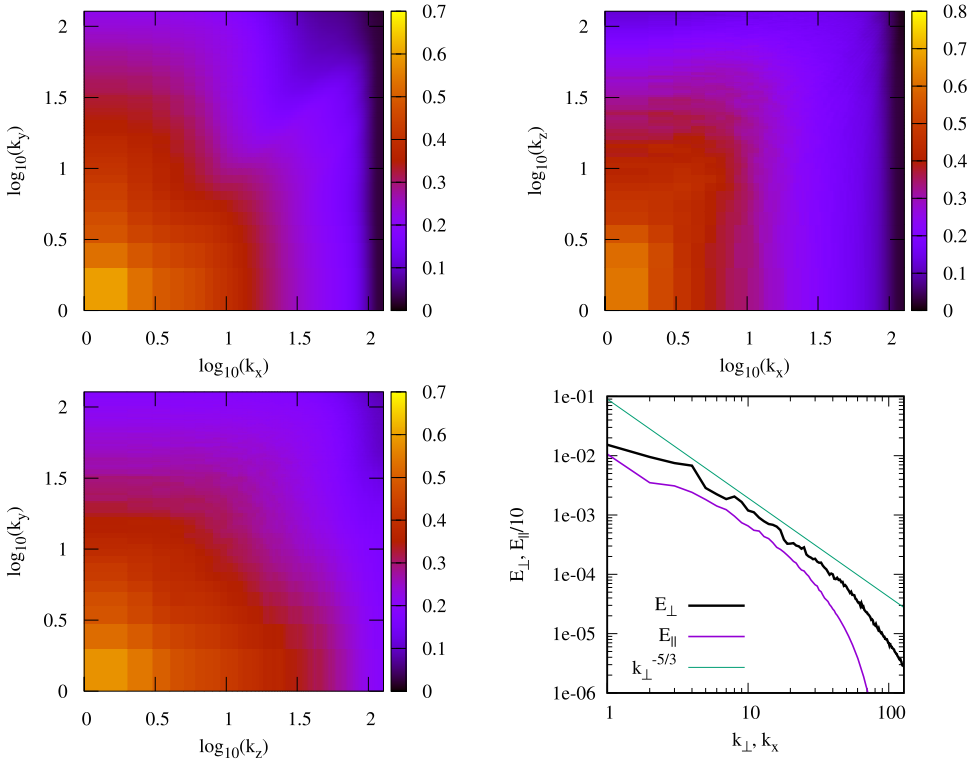

Figure 4. Contour plots of 2D magnetic spectra: $(e_{xy})^{0.5}$ in the k_x k_y plane (top-left panel); $(e_{xz})^{0.5}$ in the k_x k_z plane (top-right panel); $(e_{zy})^{0.5}$ in the k_z k_y plane (bottom-left panel). Bottom-right panel: the perpendicular $E_\perp$ (black line) and parallel $E_{||}/10$ (purple line) spectra as functions of $k_\perp$ and k_x, respectively; a function $\propto k_\perp^{-5/3}$ (green line).

axis is in the direction of the mean magnetic field $\langle \boldsymbol{B} \rangle_t$ and the rms value δB_Y is maximum (both the average and the standard deviations are calculated for the considered data sample). A comparison shows that our model qualitatively reproduces some features of the data set: the near constancy of $|\boldsymbol{B}|$; the presence of discontinuities, mainly in the B_y component, where $\boldsymbol{B}$ have abrupt rotations; and the comparative small variations in the component (B_x) that is parallel to $\langle \boldsymbol{B} \rangle$. The profiles shown in the top panel of Figure 2 are smoother than those corresponding to the solar wind data set, due to the limited spectral range extension in the model.

In Figure 3 a scatter plot of positions of the $\boldsymbol{B}$ vector tips in the 3D space is shown, along with projections onto coordinate planes. It has been obtained from a 50,000 uniformly distributed gridpoints subset. As expected, points are distributed on a portion of a spherical surface centered in the x direction and about twice wider along y than along z.

When calculating the Fourier spectrum of $\boldsymbol{B}$, in order to avoid the sharp discontinuity due to the non-periodicity in the y direction, we have doubled the extension of the spatial domain along y, imposing the "mirror" condition $\boldsymbol{B}(x, y, z) = \boldsymbol{B}(x, 2L_y - y, z)$, for $L_y \leqslant y \leqslant 2L_y$. Therefore, $\boldsymbol{B}$ is periodic with uniform intensity in the extended domain $D' = [0, L_x] \times [0, 2L_y] \times [0, L_z]$. In Figure 4 contour plots of 2D magnetic field spectra $e_{ij}(k_i, k_j) = \langle |\hat{\boldsymbol{B}}(k_i, k_j, x_n)|^2 \rangle_{x_n}$, $i \neq j \neq n$ ($\hat{\boldsymbol{B}}$ being the 2D Fourier transform of $\boldsymbol{B}$) are shown in the planes k_x k_y, k_x k_z, and k_z k_y, averaged along z, y, and x, respectively. The top panels show a clear prevalence of wavevectors (k_y and k_z) perpendicular to $\langle \boldsymbol{B} \rangle$, on parallel ($k_x$) wavevectors. This feature reproduces, at least qualitatively, what is expected for a magnetohydrodynamic (MHD) turbulence, where the cascade preferentially takes place perpendicularly to $\langle \boldsymbol{B} \rangle$ (Matthaeus et al. 1986; Carbone & Veltri 1990; Oughton et al. 1994; Snodin et al. 2013). In contrast, the spectrum is more isotropic in the transverse k_y k_z plane, with a slight prevalence of k_z wavevectors. We checked the dependence of the spectral energy on wavevectors: in the bottom-right panel the perpendicular spectrum $E_\perp(k_\perp)$ integrated in concentric shells in the k_y k_z plane and averaged along x, is plotted as a function of $k_\perp = (k_y^2 + k_z^2)^{1/2}$. The presence of a power-law range (more than one decade wide) with an index close to $-5/3$ is visible. The parallel spectrum $E_{||}(k_x)$ averaged along y and z is also plotted. $E_{||}$ does not display a clear power-law range, even if is decays faster than $E_\perp$. Therefore, the spectral energy follows the critical-balance assumption (Goldreich & Sridhar 1995), at least with its dependence on $k_\perp$.

4. Conclusions

In this Letter we have presented a numerical model of a 3D magnetic field $\boldsymbol{B}$, which reproduces several features observed in the turbulence of solar wind fast-speed streams. The model could be applied to the study of energetic particle transport in the fast solar wind with a more realistic representation of the magnetic turbulence. The model also allows us to self-consistently estimate the amplitude of the associated density fluctuations, assuming that they are driven by $|\boldsymbol{B}|$ fluctuations. Another possible application is the study of the parametric instability of a 3D turbulent Alfvénic state, characterized by uniform-intensity magnetic and velocity fields. In this context, only 1D or 2D configurations have been considered so far (see,

e.g., Primavera et al. (2019) and references therein), while the 3D case would be more appropriate for solar wind.

In our model, the intensity $|\boldsymbol{B}|$ is remarkably uniform in the spatial domain, the normalized rms variation being $\delta|\boldsymbol{B}|/B_T \sim 0.1\%$. Using a different method, Roberts (2012) obtained a value that is ∼50 times larger. This feature is important for parametric instability studies, because the unperturbed Alfvénic state propagates without distortions only if $|\boldsymbol{B}|$ is uniform (Primavera et al. 2019). We found that singularities are present in the form of rotational discontinuities with associated current sheets that extend in the 3D domain. This feature seems to be present regardless of the particular choice of A_x, A_y, and of the boundary condition a_z. Of course, our method selects a particular class of solutions and our results do not represent a rigorous proof that rotational discontinuities must necessarily be present in any uniform-intensity magnetic field. However, the same property has been found independently by Roberts (2012), strongly suggesting that rotational discontinuities are related to the uniformity of $|\boldsymbol{B}|$. In our case, the mechanism generating such singularities is related to the nonlinearity of Equation (1), which enforces the condition $|\boldsymbol{B}| =$ uniform.

The magnetic field spectra are anisotropic, with a prevalence of wavevectors perpendicular to $\langle \boldsymbol{B} \rangle$ on parallel wavevectors. This feature, which is qualitatively in accordance with MHD turbulence expectations, is at least partially induced by the anisotropic spectrum imposed for the spatial derivatives of vector potential components A_x and A_y. As a function of $k_\perp$ the spectrum has a power-law range, with an index compatible with the Kolmogorov spectrum. No clear power-law range is present in the parallel spectrum, though it decays faster than $E_\perp$.

In conclusion, the present model, within its own limitations, is a good representation of 3D solar wind turbulence in fast-speed, nearly incompressible streams, which could be used to obtain new insights in physical processes taking place in space plasmas.

We are grateful to Prof. Berardino Sciunzi for many useful discussions on the subject of this Letter.

ORCID iDs

Francesco Valentini https://orcid.org/0000-0002-1296-1971
Francesco Malara https://orcid.org/0000-0002-5554-8765
Luca Sorriso-Valvo https://orcid.org/0000-0002-5981-7758
Roberto Bruno https://orcid.org/0000-0002-2152-0115

References

Barnes, A. 1981, JGR, 86, 7498
Barnes, A., & Hollweg, J. V. 1974, JGR, 79, 2302
Bavassano, B., Pietropaolo, E., & Bruno, R. 2000a, in Proc. 9th European Meeting on Solar Physics, On the Radial Decrease of Alfvénic Fluctuations in the Polar Wind, in Magnetic Fields and Solar Processes, ed. A. Wilson (Noordwijk: ESA), 1135
Bavassano, B., Pietropaolo, E., & Bruno, R. 2000b, JGR, 105, 15959
Belcher, J. W., & Davis, L. 1971, JGR, 76, 3534
Bruno, R., Bavassano, B., & Villante, U. 1985, JGR, 90, 4373
Bruno, R., & Carbone, V. 2013, LRSP, 2, 4
Bruno, R., Carbone, V., Primavera, L., et al. 2004, AnGeo, 22, 3751
Bruno, R., Telloni, D., Sorriso-Valvo, L., et al. 2019, A&A, 627, A96
Carbone, V., & Veltri, P. 1990, GApFD, 52, 153
Cohen, R. H., & Kulsrud, R. M. 1974, PhFl, 17, 2215
Del Zanna, L. 2001, GeoRL, 28, 2585
Del Zanna, L., Matteini, L., Landi, S., Verdini, A., & Velli, M. 2015, JPlPh, 81, 325810102
Goldreich, P., & Sridhar, S. 1995, ApJ, 438, 763
Juneja, A., Lathrop, D. P., Sreenivasan, K. R., & Stolovitzky, G. 1994, PhRvE, 49, 5179
Lele, S. K. 1992, JCoPh, 103, 16
Malara, F., Di Mare, F., Nigro, G., & Sorriso-Valvo, L. 2016, PhRvE, 94, 053109
Malara, F., & Elaoufir, J. 1991, JGR, 96, 7641
Malara, F., Primavera, L., & Veltri, P. 2000, PhPl, 7, 2866
Malara, F., Primavera, L., & Veltri, P. 2001, NPGeo, 8, 159
Malara, F., & Velli, M. 1996, PhPl, 3, 4427
Matteini, L., Horbury, T. S., Neugebauer, M., & Goldstein, B. E. 2014, GeoRL, 41, 259
Matteini, L., Horbury, T. S., Pantellini, F., Velli, M., & Schwarzt, S. J. 2015, ApJ, 802, 11
Matteini, L., Landi, S., Del Zanna, L., Velli, M., & Hellinger, P. 2010, GeoRL, 37, L20101
Matteini, L., Stansby, D., Horbury, T. S., & Chen, C. H. K. 2018, ApJL, 869, L32
Matthaeus, W. H., Goldstein, M. L., & King, J. H. 1986, JGR, 91, 59
Meneveau, C., & Sreenivasan, K. R. 1987, PhRvL, 59, 1424
Oughton, S., Priest, E. R., & Matthaeus, W. H. 1994, JFM, 280, 95
Perri, S., Valentini, F., Sorriso-Valvo, L., Reda, A., & Malara, F. 2017, P&SS, 140, 6
Primavera, L., Malara, F., Servidio, S., et al. 2019, ApJ, in press
Pucci, F., Malara, F., Perri, S., et al. 2016, MNRAS, 459, 3395
Riley, P., Sonnet, C. P., Balogh, A., et al. 1996, JGR, 101, 19987
Roberts, D. A. 2012, PhRvL, 109, 231102
Rosales, C., & Meneveau, C. 2006, PhFl, 18, 075104
Sardina, G., Picano, F., Brandt, L., & Caballero, R. 2015, PhRvL, 115, 184501
Saur, J., & Bieber, J. W. 1999, JGR, 104, 9975
Shoda, M., Yokoyama, T., & Suzuki, T. K. 2018, ApJ, 860, 17
Snodin, A. P., Ruffolo, D., Oughton, S., Servidio, S., & Matthaeus, W. H. 2013, ApJ, 779, 56
Tenerani, A., & Velli, M. 2013, JGRA, 118, 7507
Tenerani, A., & Velli, M. 2018, ApJL, 867, L26
Tsurutani, B. T., & Ho, C. M. 1997, RvGeo, 37, 517
Vasquez, B. J., & Hollweg, J. V. 1998, JGR, 103, 335
Wicks, R. T., Mallet, A., Horbury, T. S., et al. 2013, PhRvL, 110, 025003